Electronic Supplementary Material (ESI) for Sustainable Energy & Fuels.

Supporting Information

Ammonia-etching-assisted nanotailoring of manganese silicate boost faradic capacity for high-performing hybrid supercapacitors

Xueying Dong [1], Yifu Zhang[1]*, Qiang Chen[2], Hanmei Jiang[1], Qiushi Wang[1], Changgong Meng[1], Zongkui Kou[2]*

1. *School of Chemical Engineering, Dalian University of Technology, Dalian 116024, PR China*
2. *Department of Materials Science and Engineering, National University of Singapore, 117574, Singapore.*

*E-mail address: yfzhang@dlut.edu.cn (Y. Zhang) or msekz@nus.edu.sg (Z. Kou)

EXPERIMENTS

Materials

Tetraethyl orthosilicate (TEOS, $[Si(OC_2H_5)_4]$), ammonium hydroxide ($NH_3 \cdot H_2O$, 25 wt%), manganese acetate ($Mn(OAc)_2 \cdot 4H_2O$), nickel foam, acetylene black, N-methyl-2-pyrrolidone (NMP, C_5H_9NO), polyvinylidene fluoride (PVDF, $-(CH_2-CF_2)_n-$), graphite flakes with an average diameter of 37.4 microns, polyvinyl alcohol ($[C_2H_4O]_n$) with an average molecular weight of 1799, and potassium hydroxide (KOH) were purchased from Aladin Chemical Reagent Co., Ltd. All the chemicals were used directly without any further purification.

Synthesis of SiO_2 spheres

SiO_2 spheres with a diameter of ~200 nm were prepared based on a modified StÖber method[1]. 2.5 mL TEOS $[Si(OC_2H_5)_4]$ was dripped into 46 mL ethanol solution (CH_3CH_2OH) at a uniform dropping rate and stirred for 10 minutes at high speed at room temperature. Then 5 mL ammonium hydroxide ($NH_3 \cdot H_2O$) was added drop by drop, and the system was turned into uniformly milky. After 4 h of reaction, the solution was centrifuged for 3 times with ethanol and deionized water, and the white paste was dried in the vacuum oven at 60 ℃ for 36 h. The product was white powder with uniform particle size of about 200 nm (Figure S1a b and c)[2].

Synthesis of GO

The preparation method of GO was according to a modified Hummer's method[2], which was mainly divided into three stages: low temperature stage, medium temperature stage and high temperature stage. Low temperature stage: according to take 2 g graphite, 1g $NaNO_3$, 46 mL H_2SO_4, put them in 500 mL beaker, ice bathing, ultrasonic within 15 min until the beaker of solution temperature below 3 °C, transferred them to the ice bath pot then slowly added 6 g $KMnO_4$, stirring for 1 h to get blackening solution, the edge of the solution for the dark green; Medium temperature stages: under the condition of 35 °C water bath mixing 1 h, the solution getting into viscous significantly. High temperature stages: adding in 92 mL deionized water inside the beaker, the solution into brown, in 90 °C water bath stirring for 15 min after, then pour into 300 mL deionized water, 10 mL 30% H_2O_2 in turn, stirring for 10 min after delamination, for the gold at the top, bottom was black, poured out on the yellow clear liquid and added 10 mL of the mass fraction of 10% HCl, stirring again let stand for 12 h after stratification, poured out the gold solution at the top that adding deionized water until the upper supernatant fluid yellow became not obvious at this time no longer with deionized water, the GO solution was successfully prepared and turned the solution to the brown bottle for use[3], The morphology of GO is nanosheets[2], as shown in Figure S1d.

Synthesis of α-manganese silicate (nt-$MnSiO_3$)

The nt-manganese silicate (nt-$MnSiO_3$) nanoparticles were prepared using SiO_2 microspheres as silicon source by an etching technology combined with an in-situ hydrothermal method, as shown in Scheme 1. In detail, 0.05 g SiO_2 microspheres were dissolved in 10 mL deionized water with magnetic stirring for 30 minutes (Solution A). 0.4080 g of manganese acetate ($Mn(OAc)_2 \cdot 4H_2O$) was dissolved in 10 mL water with magnetic stirring for 15 minutes (Solution B). And then, 0.25 mL ammonium hydroxide, Solution A and Solution B were mixed (the pH of the solution was about 9.04), stirred for 30 minutes and transferred to 40 mL Teflon-lined stainless steel autoclave and kept at 180 ℃ for 12 h. After the reaction, the products were filtered off, washed with distilled H_2O and absolute ethanol several times to remove any possible residues, and dried in vacuum at 75 °C overnight to obtain nt-$MnSiO_3$ nanoparticles (Figure S2). The chemical reactions in this process can be summarized as follows:

$$SiO_2 + 2OH^- \leftrightarrow SiO^{2-}_{3} + H_2O \tag{S1}$$

$$Mn^{2+} + 6NH_3 \cdot H_2O \leftrightarrow [Mn(NH_3)_6]^{2+} + 6H_2O \tag{S2}$$

$$[Mn(NH_3)_6]^{2+} + SiO^{2-}_{3} + 6H_2O \leftrightarrow MnSiO_3 + 6NH_3 \cdot H_2O \tag{S3}$$

During the experiments, considering to get the highest capacitance, the influence of the atomic ratio of Mn/Si on the electrochemical properties of nt-$MnSiO_3$ was first studied and the quantity of $Mn(OAc)_2 \cdot 4H_2O$ was fixed to 0.2040 g, 0.3060 g, 0.4080 g and 0.6119 g (0.05 g of SiO_2) using the same route. These samples were named as nt-$MnSiO_3$-1, nt-$MnSiO_3$-2, nt-$MnSiO_3$-3 and nt-$MnSiO_3$-4, respectively. It was found that the sample nt-$MnSiO_3$-3 in the recipe showed the best electrochemical performance (Figures S3-S6). Thus, the sample nt-$MnSiO_3$-3 was chosen to synthesize the following samples.

Synthesis of nt-$MnSiO_3$ yolk-hollow spheres (ys-$MnSiO_3$)

The synthesis process of ys-$MnSiO_3$ spheres is the same as nt-$MnSiO_3$ nanoparticles except that ammonia was not added.

Synthesis of nt-$MnSiO_3$/reduced graphene oxide (nt-$MnSiO_3$/rGO) composite)

0.1 g of nt-$MnSiO_3$-3 were dispersed to 20 mL deionized water by ultrasound for 30 minutes (Solution C). 3 mL of GO solution (concentration: 6.7 $g \cdot L^{-1}$) was dispersed to 20 mL deionized water for uniform ultrasonic dispersion (Solution D). The Solution C and Solution D were mixed with magnetic stirring for 12 h and freeze-dried to obtain nt-$MnSiO_3$/GO composite. At last, the nt-$MnSiO_3$/GO composite was calcined in a muffle furnace at 280 ℃ for 1 h to get nt-$MnSiO_3$/rGO composite.

To study the influence of GO on the electrochemical properties of nt-$MnSiO_3$-3 composite, the volume of GO solution fixed to 0.75 mL, 1.5 mL, 3 mL and 6 mL (0.1 g of nt-$MnSiO_3$-3) using the same route. These samples were named as nt-$MnSiO_3$/rGO-1, nt-$MnSiO_3$/rGO-2, nt-$MnSiO_3$/rGO-3 and nt-$MnSiO_3$/rGO-4, respectively. It was found that the sample nt-$MnSiO_3$/rGO-3 in the recipe showed the best electrochemical performance discussed in the paper.

Materials characterizations

The phase was confirmed by X-ray powder diffraction (XRD) using Panalytical X'Pert powder diffractometer and Cu-Kα (λ = 0.15418 nm) X-ray source operated at 45 kV and 100 mA, at a rate of 5º min^{-1} from 5 to 80°. The chemical composition was revealed by an energy-dispersive X-ray spectrometer (EDS) and elemental mappings attached to a scanning electron microscope (SEM, QUANTA450). X-ray photoelectron spectroscopy (XPS) was performed on ESCALAB250Xi, Thermo Fisher Scientific. Fourier transform infrared spectroscopy (FTIR) pattern was measured using KBr pellet technique and recorded on a Nicolet 6700 spectrometer from 4000 to 400 cm^{-1} with a resolution of 4 cm^{-1}. Raman spectrum was characterized by a Thermo Scientific spectrometer, with a 532 nm excitation line. The morphology was identified by field emission scanning electron microscopy (FE-SEM, NOVA NanoSEM 450, FEI) and transmission electron microscopy (TEM, FEITecnai F30). The sample for FE-SEM observation was gold-sputtered to get better morphology, and it was dispersed in absolute ethanol with ultrasonication before TEM test. The surface area was determined by Brunauer-Emmet-Teller (BET) method using Micromeritics ASAP-2020 and the samples were degassed at 150 °C for several hours. Pore volume and average pore size were calculated by Barrett-Joyner-Halenda (BJH) formula.

Electrode preparation and electrochemical measurements

The working electrodes were prepared using a mixture of 80 wt% of the as-synthesized active materials, 10 wt% of polyvinylidene difluoride (PVDF) and 10 wt% of carbon black, and N-methyl-2-pyrrolidone (NMP) was used as a solvent. The mixed slurries were coated onto Ni foils and heated at 80 °C overnight to remove the organic solvent. Then these foils were pressed onto Ni-grids (1 cm^2) at a pressure of 10 MPa. The mass of active substance loading was about 3~4 mg cm^{-2} (For nt-$MnSiO_3$-1, nt-$MnSiO_3$-2, nt-$MnSiO_3$-3 and nt-$MnSiO_3$-4, the specific loading are 0.00328, 0.00364, 0.00392 and 0.00308 g respectively; For nt-$MnSiO_3$/rGO-1, nt-$MnSiO_3$/rGO-2, nt-$MnSiO_3$/rGO-3 and nt-$MnSiO_3$/rGO-4, the specific loading are 0.00348, 0.00304, 0.0033 and 0.003 g respectively; For ys-$MnSiO_3$ and rGO the specific loading are 0.00388 and 0.00324 g respectively). The electrolytes were used 3.0 M KOH solution. Cycling voltammetry (CV), galvanostatic charge-discharge (GCD) and electrochemical impedance spectroscopy (EIS) were used to investigate the electrochemical performance of the electrode materials. The typical three electrode experimental cell was equipped with a carbon rod and mercury oxide electrode (Hg-HgO) as the counter electrode and reference electrode, respectively. The electrochemical measurements were carried out on a CHI-660D electrochemical work station. The voltage window of the optimal capacitance of nt-$MnSiO_3$-3 and nt-$MnSiO_3$/rGO-3 is ranging from -0.6 V to 0.5 V (Figure S3). The specific capacitance (C, F g^{-1}) and specific capacity (Q_p, C g^{-1}) of the active material in the electrode determined using charge-discharge curves can be calculated from the following Equation S4 and S5:

$$C = \frac{I \cdot \Delta t}{m \cdot \Delta V} \tag{S4}$$

$$Q_p = \frac{I \cdot \Delta t}{m} \tag{S5}$$

Where C (F g^{-1}) is the specific capacitance, Q_p (C g^{-1}) represents the specific capacity, I (A) is the discharge current, Δt (s) is the discharge time, m (g) is the mass of the active material in the working electrode, ΔV (V) represents the potential drop during the discharge process.

The hybrid supercapacitors (HSCs) device was assembled using active material nt-$MnSiO_3$/rGO-3 as the positive electrode, activated carbon (AC) as the negative electrode, and PVA/KOH as the electrolyte, denoted as nt-$MnSiO_3$/rGO//AC HSC device. The mass of the nt-$MnSiO_3$/rGO-3 and AC in the electrodes of HSC device is matched by Equation (9), the specific value are $m_{+(nt-MnSiO3/rGO-3)} =$ 0.008 g; $C_{+(nt-MnSiO3/rGO-3)} =$ 860 F g^{-1}; $m_{-(AC)} =$ 0.04 g; $C_{-(AC)} =$ 160 F g^{-1}

$$Q_+ = Q_- = m_+ * C_+ = m_- * C_- \tag{9}$$

The coating area of the active substance was 1 cm * 2 cm. The PVA/KOH electrolyte was made by 3.04 g PVA and 4.2 g KOH dissolved in 30 mL deionized water at 85 °C. The water system membrane was immersed and put into the positive and negative electrode sheets, and the device was insulated from the air by the thermal sealing with polyethylene plastic film. The energy density E (W h kg^{-1}) and power density P (W kg^{-1}) of the device can be calculated according to the equation (S6) and (S7), respectively. Please note the conversion of the unit during the Equation S6 and S7.

$$E = \frac{1}{2} C \cdot (\Delta V)^2 \tag{S6}$$

$$P = \frac{E}{\Delta t} \tag{S7}$$

The StÖber SiO_2 spheres were prepared by condensation dehydration/dealcoholization of silicate acid which obtained by hydrolysis of tetraethyl silicate[4-7]. There are a large number of active hydroxyl groups on the surface of StÖber SiO_2 spheres, which equipped with relatively high reaction energy under hydrothermal conditions. This results in the partial dissolution of SiO_2 spheres surface to obtain a small amount of SiO_3^{2-} and then combined with $[Mn(NH_3)_6]^{2+}$ to obtain α-$MnSiO_3$ coated on the surface of microspheres. With the progress of the reaction, the particle size of the inner SiO_2 spheres decreases, making the surface energy slightly higher than that of the unreacted microsphere. But the diffusion speed of $[Mn(NH_3)_6]^{2+}$ from the solution to the SiO_2 sphere's surface also decreases as the concentration goes down, and finally, the two processes are stable to α-$MnSiO_3$ shell and unreacted SiO_2 core with yolk-hollow structure.

Figures S7 and S8 show CV at different scan rates and GCD curves at different current densities of nt-$MnSiO_3$-1, nt-$MnSiO_3$-2, nt-$MnSiO_3$-3 and nt-$MnSiO_3$-4, and Figure S9 summarizes the corresponding results to compare their electrochemical properties. Combined the enclosed area of CV curves at the scan rate of 20 mV s^{-1} (Figure S9a) with the charging and discharging time of GCD curves at the current density of 0.5 A g^{-1} (Figure S9b), it can be found that the nt-$MnSiO_3$-3 possesses the best capacitance of 167 F g^{-1} (184 C g^{-1}) at 0.5 A g^{-1} among nt-$MnSiO_3$-1, nt-$MnSiO_3$-2, nt-$MnSiO_3$-3 and nt-$MnSiO_3$-4. The relevance between the specific capacity and the current densities of nt-$MnSiO_3$-1, nt-$MnSiO_3$-2, nt-$MnSiO_3$-3 and nt-$MnSiO_3$-4 is summarized in Figure S9c from GCD curves (Figure S8). It is shown that the α-$MnSiO_3$-3 exhibits the optimal specific capacitance.

Figures S10 and S11 show CV at different scan rates and GCD curves at different current densities of nt-$MnSiO_3$/rGO-1, nt-$MnSiO_3$/rGO-2, nt-$MnSiO_3$/rGO-3 and nt-$MnSiO_3$/rGO-4, and Figure S12 summarizes the corresponding results to compare their electrochemical properties. Combined the enclosed area of CV curves at the scan rate of 20 mV s^{-1} (Figure S12a) with the charging and discharging time of GCD curves at the current density of 0.5 A g^{-1} (Figure S12b), it can be found that the nt-$MnSiO_3$/rGO-3 possesses the best capacitance of 860 F g^{-1} (946 C g^{-1}) at 0.5 A g^{-1} among nt-$MnSiO_3$/rGO-1, nt-$MnSiO_3$/rGO-2, nt-$MnSiO_3$/rGO-3 and nt-$MnSiO_3$/rGO-4. The relevance between the specific capacity and the current densities of nt-$MnSiO_3$/rGO-1, nt-$MnSiO_3$/rGO-2, nt-$MnSiO_3$/rGO-3 and nt-$MnSiO_3$/rGO-4 is summarized in Figure S12c from GCD curves (Figure S11). It is obviously shown that the nt-$MnSiO_3$/rGO-3 exhibits the optimal specific capacitance.

The CV curve (Figure S14a) of rGO is almost rectangular and there is no oxidation-reduction peak within this voltage range. The sharp peak at about 0.4 V is attributed to the electrolysis of water caused by the excessive applied voltage on the rGO, which indicates that rGO is a typical double-layer capacitor material, and provides a part of the double-layer capacitor in nt-$MnSiO_3$/rGO-3 system. The GCD curves (Figure S14b) of rGO present a very asymmetric state. The specific capacitance of rGO are 133 F g^{-1} at 0.5 A g^{-1}. It shows that rGO does not bring significant electrical specifications in the KOH system, which is the same as nt-$MnSiO_3$. However, the synergistic effect brought by the combination of nt-$MnSiO_3$ and rGO can greatly improve the electrical capacity.

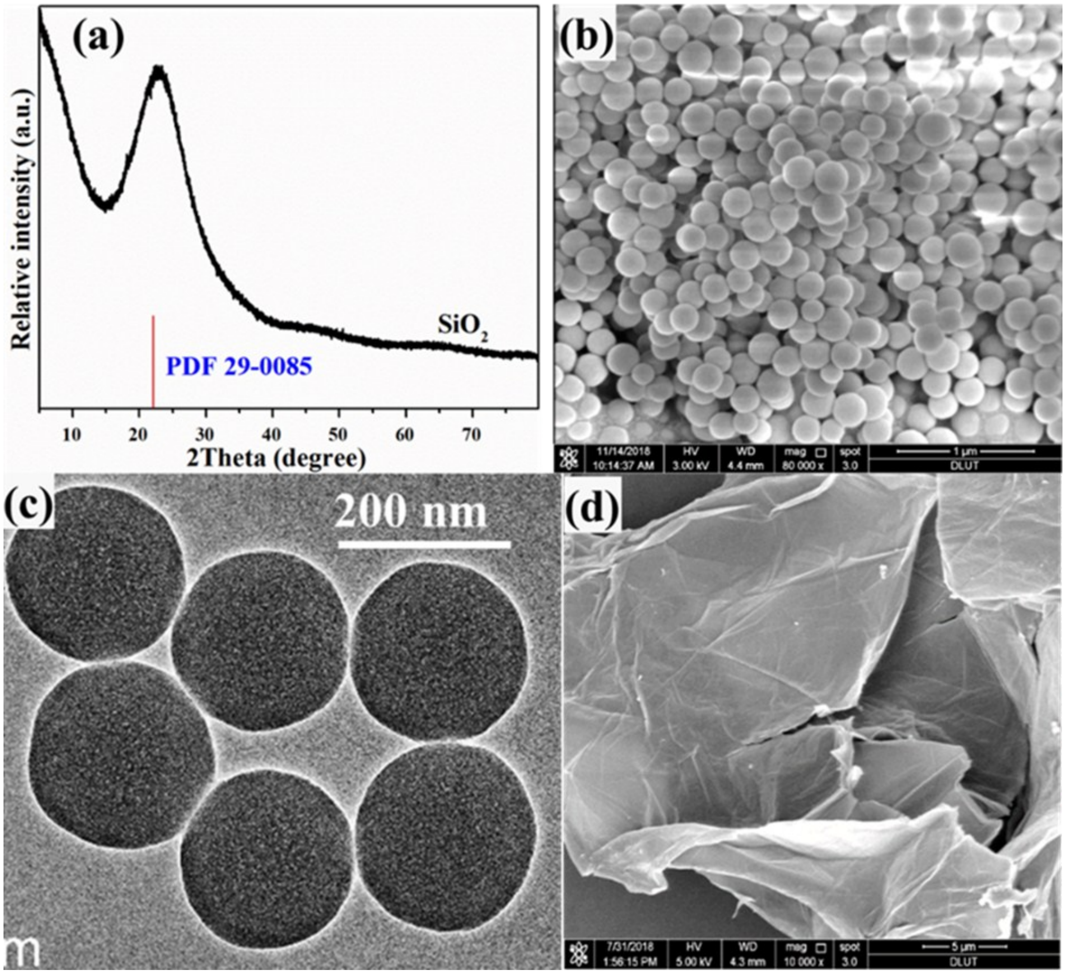

Figure S1. The XRD pattern (a), SEM image (b) and TEM image (c) of SiO_2 spheres; (d) SEM image of GO.

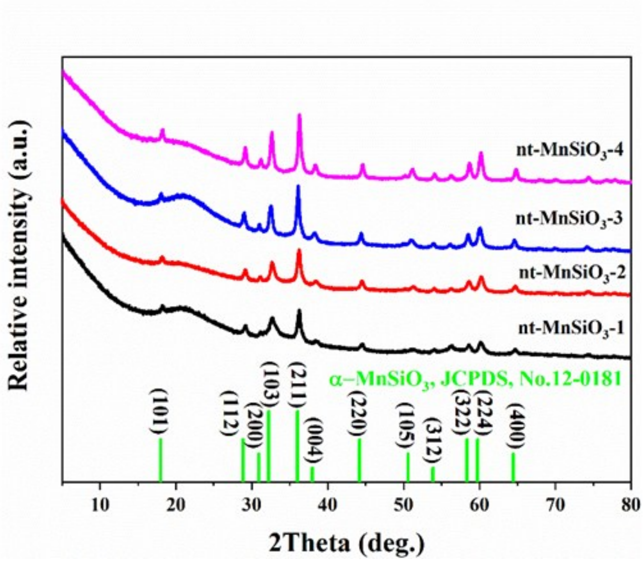

Figure S2. XRD patterns of nt-$MnSiO_3$-1, nt-$MnSiO_3$-2, nt-$MnSiO_3$-3 and nt-$MnSiO_3$-4.

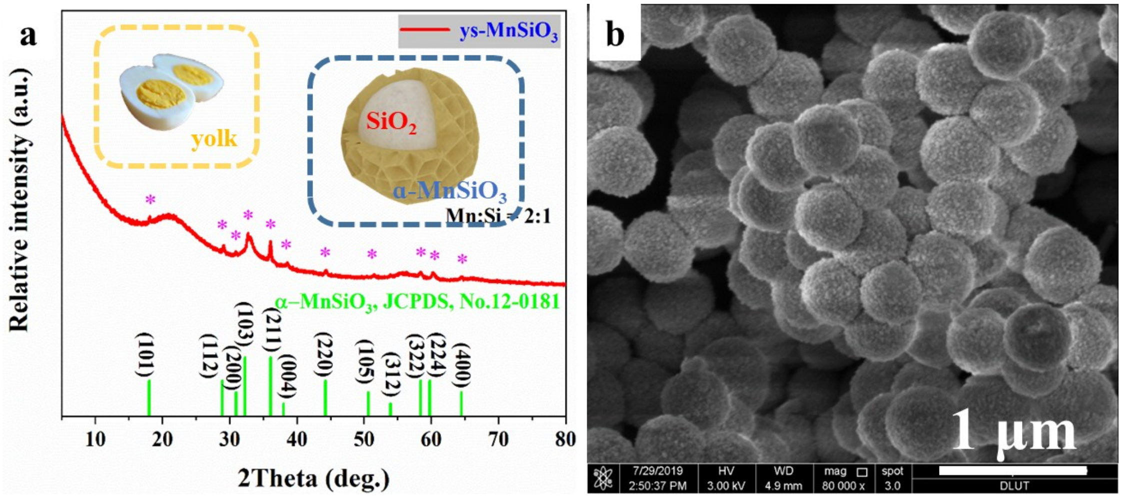

Figure S3. XRD patterns (a) and SEM (b) image of ys-$MnSiO_3$ spheres (α-$MnSiO_3$ shell on the surface and SiO_2 core inside).

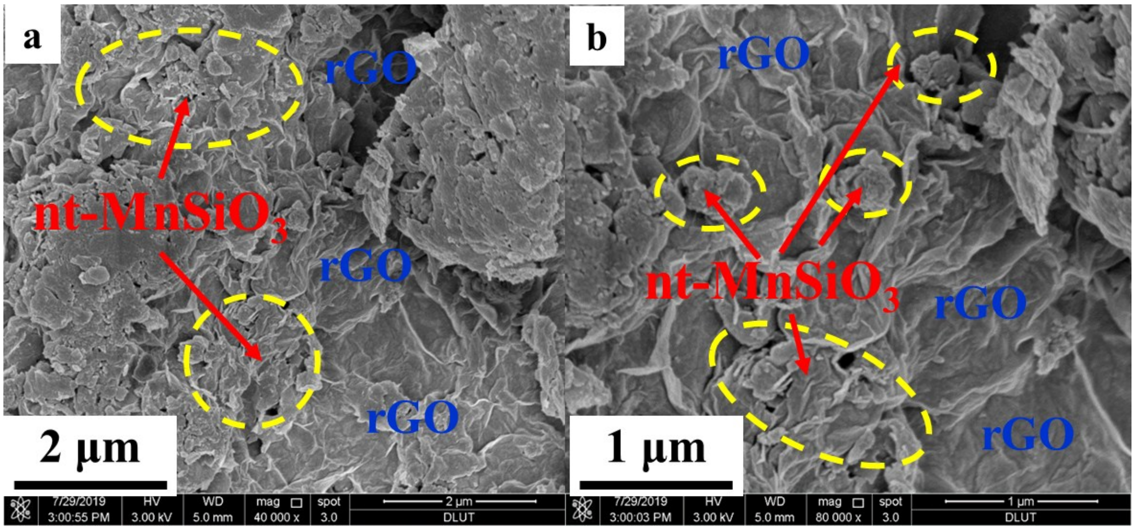

Figure S4. SEM images of nt-$MnSiO_3$/rGO.

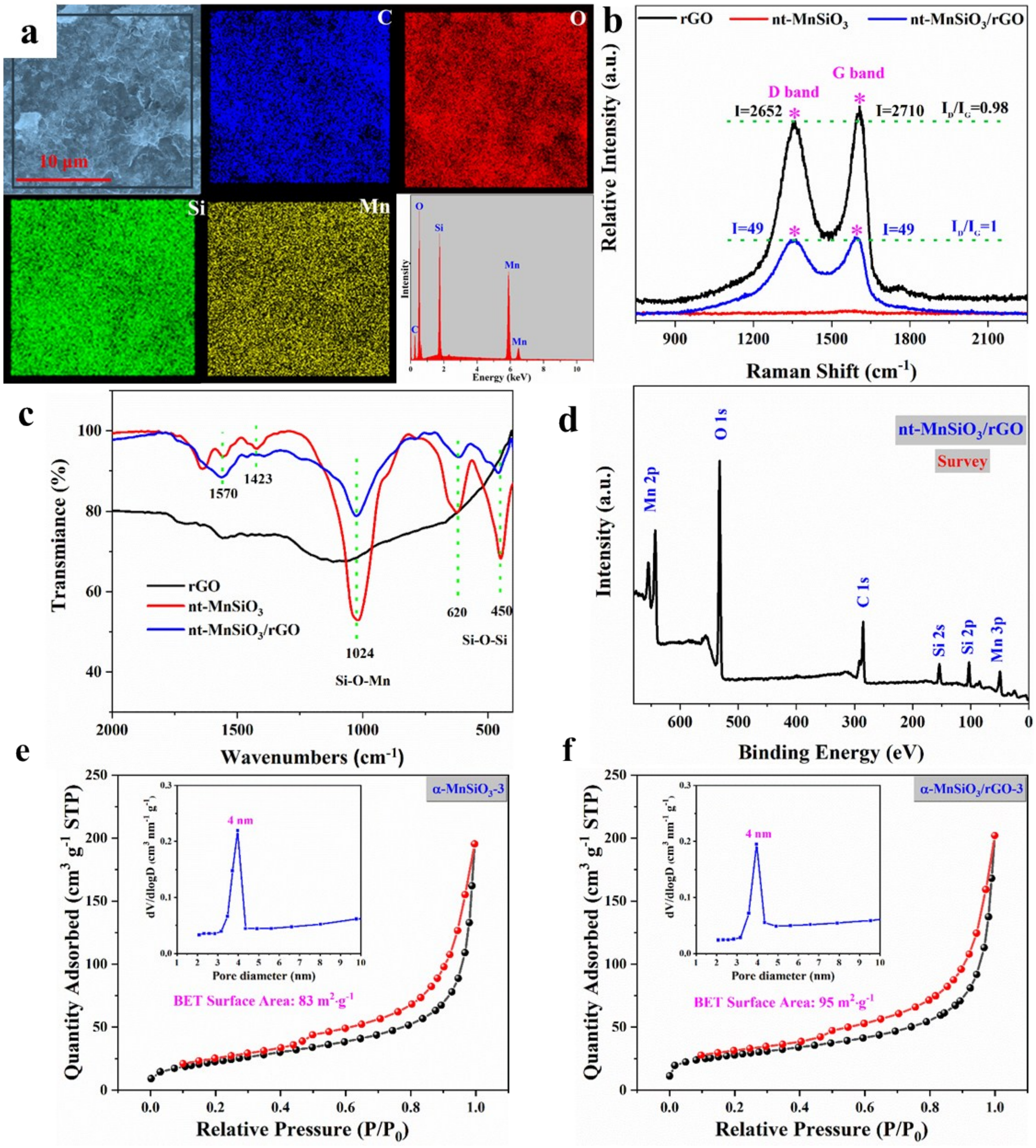

Figure S5. (a) EDS elemental mapping images and EDS spectrum of nt-$MnSiO_3$/rGO; (b) Raman and (c) FTIR spectra of rGO, nt-$MnSiO_3$and nt-$MnSiO_3$/rGO; (d) the survey of XPS of nt-$MnSiO_3$/rGO. Nitrogen adsorption and desorption isotherms and pore distribution curves of nt-$MnSiO_3$ (e) and nt-$MnSiO_3$/rGO (f).

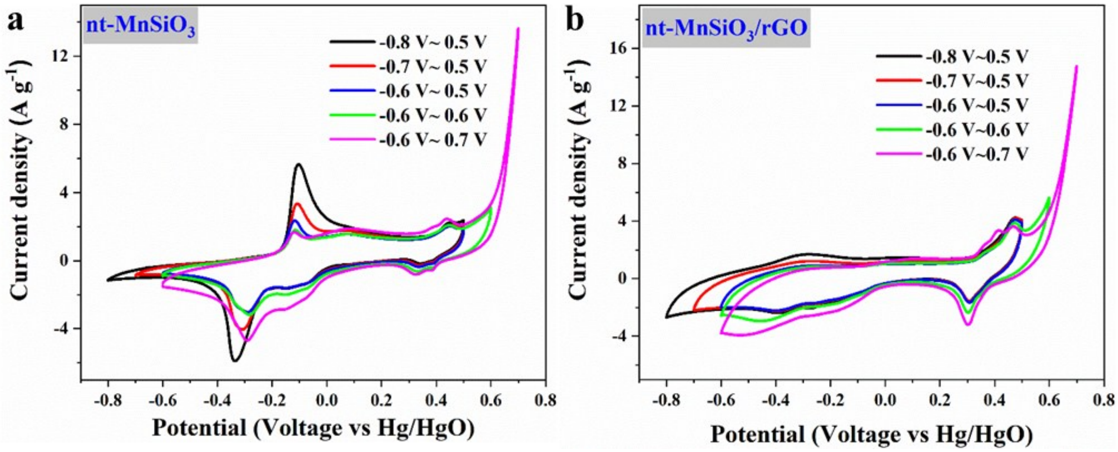

Figure S6. CV curves of nt-MnSiO3 and nt-MnSiO$_3$/rGO on various potential limits at the scan rate of 20 mV·s^{-1}. The results prove the optimal voltage window is from −0.6 V to 0.5 V.

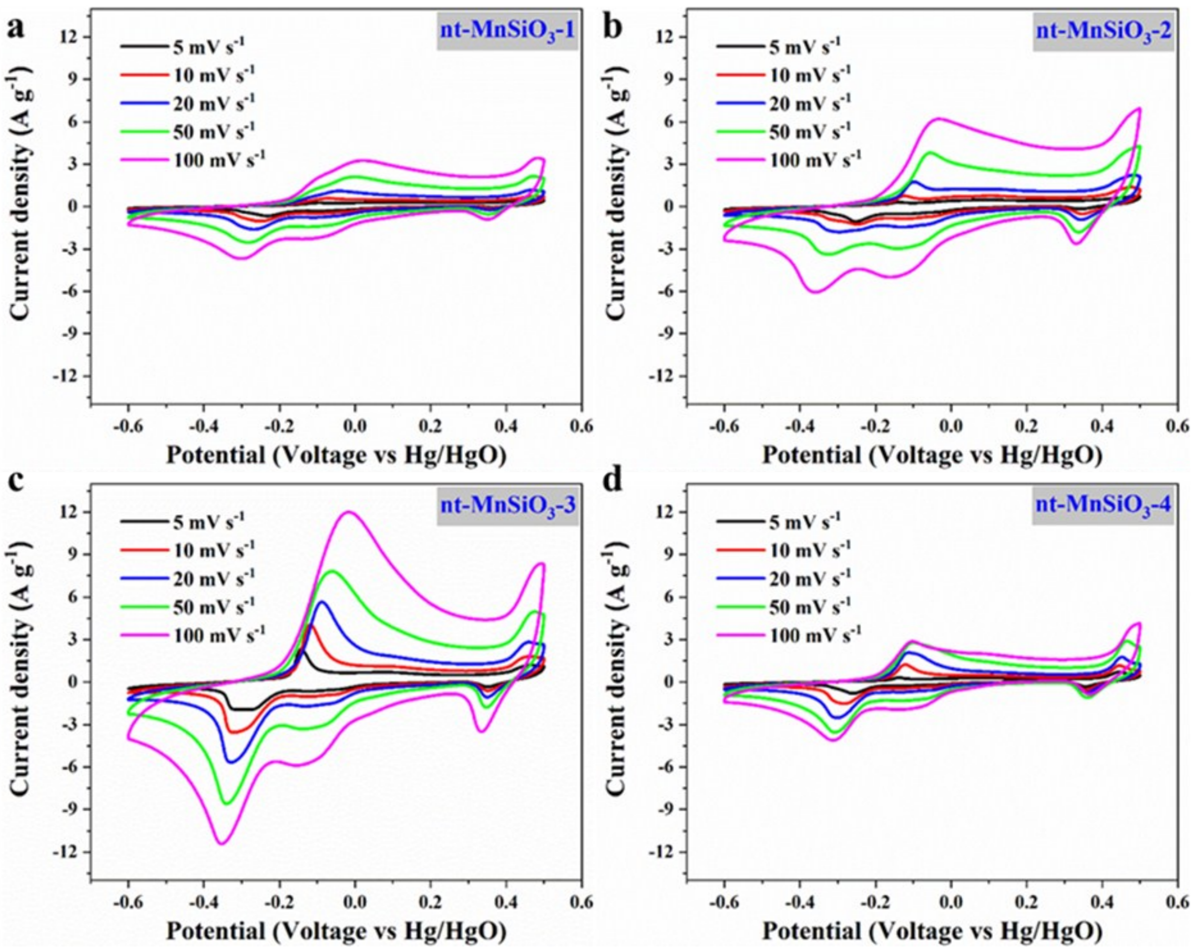
a
nt-MnSiO₃-1
b
nt-MnSiO₃-2
c
nt-MnSiO₃-3
d
nt-MnSiO₃-4
5 mV s⁻¹
10 mV s⁻¹
20 mV s⁻¹
50 mV s⁻¹
100 mV s⁻¹
Current density (A g⁻¹)
Potential (Voltage vs Hg/HgO)
12
9
6
3
0
-3
-6
-9
-12
-0.6
-0.4
-0.2
0.0
0.2
0.4
0.6

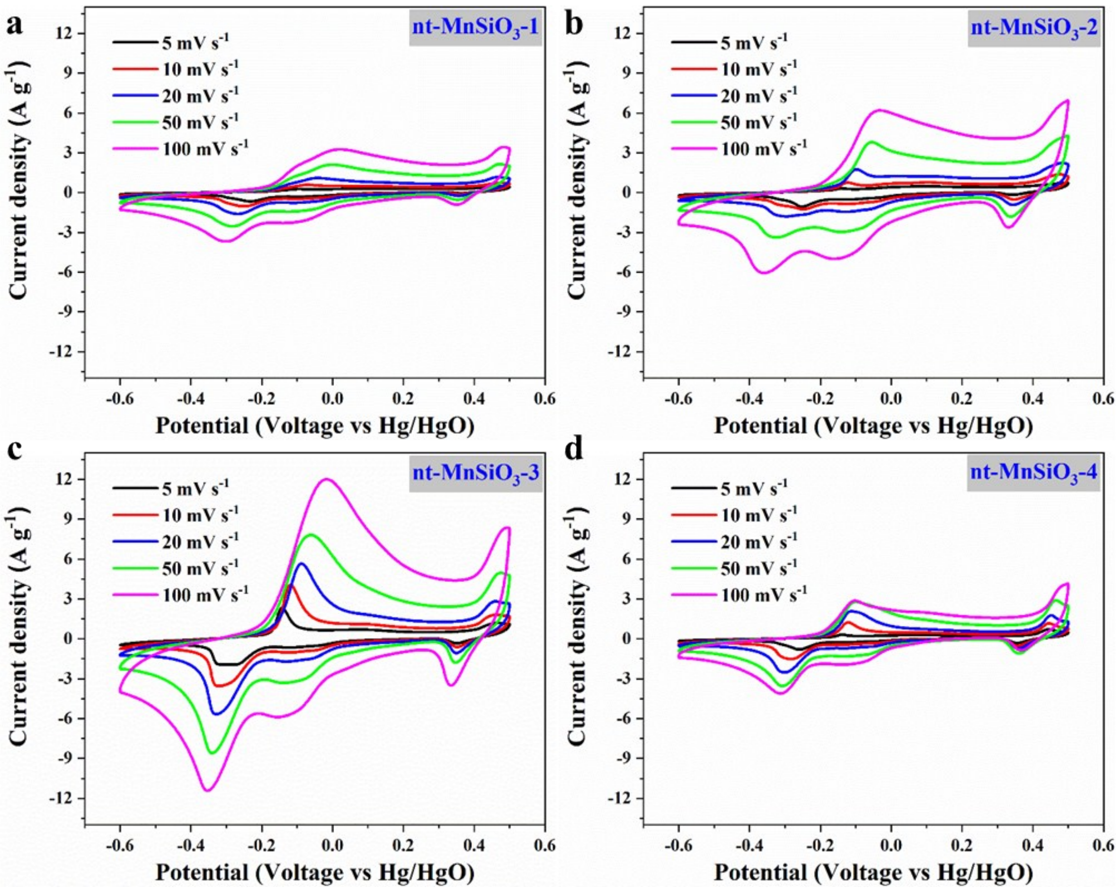

Figure S7. CV curves of nt-$MnSiO_3$-1, nt-$MnSiO_3$-2, nt-$MnSiO_3$-3 and nt-$MnSiO_3$-4 at different scan rates.

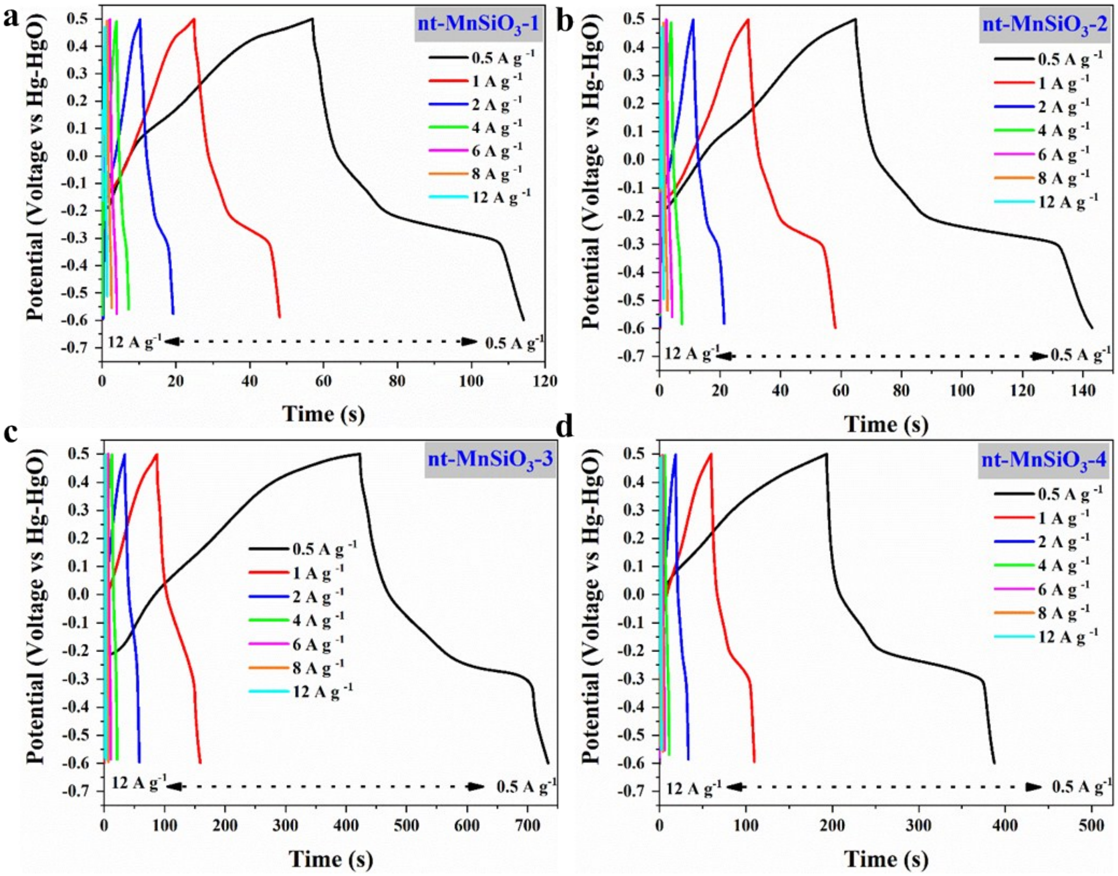

Figure S8. GCD curves of nt-$MnSiO_3$-1, nt-$MnSiO_3$-2, nt-$MnSiO_3$-3 and nt-$MnSiO_3$-4 at different current densities.

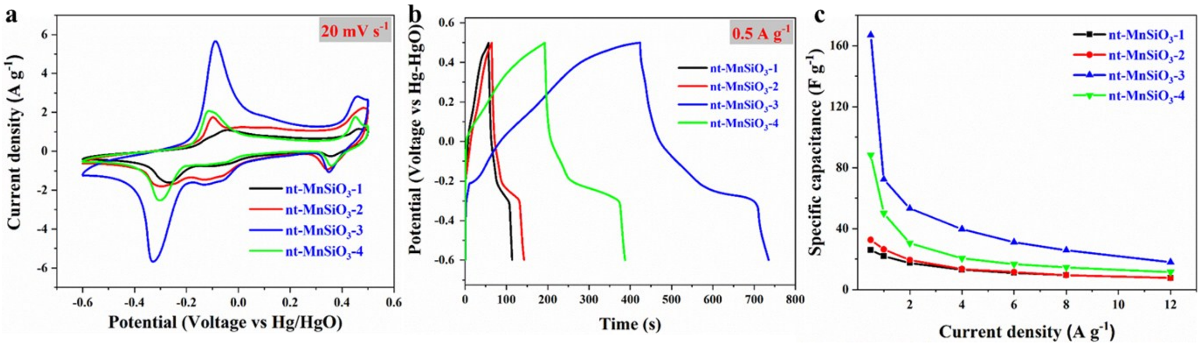

Figure S9. (a) CV curves at 20 mV·s^{-1}, (b) GCD curves at 0.5 A·g^{-1} and (c) the relationship between specific capacitance and current density based on Figure S8 of nt-$MnSiO_3$-1, nt-$MnSiO_3$-2, nt-$MnSiO_3$-3 and nt-$MnSiO_3$-4.

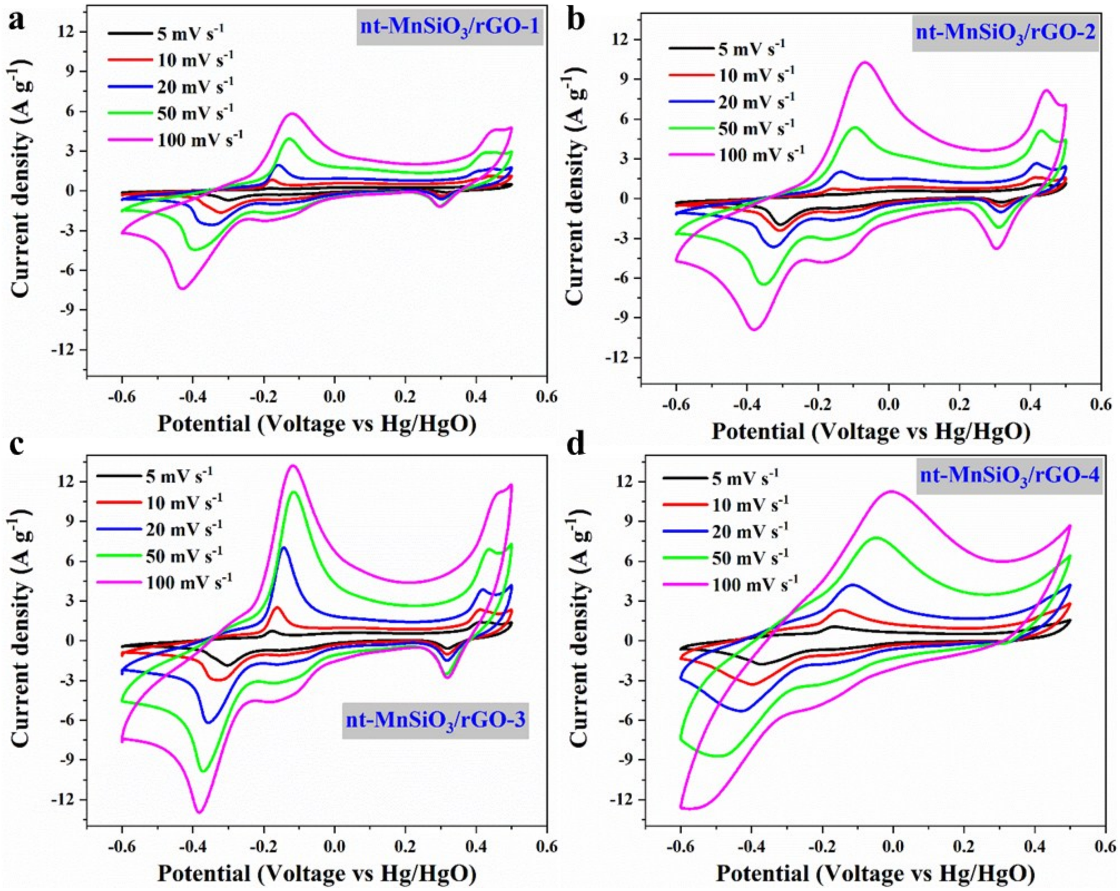

Figure S10. CV curves of nt-$MnSiO_3$/rGO-1, nt-$MnSiO_3$/rGO-2, nt-$MnSiO_3$/rGO-3 and nt-$MnSiO_3$/rGO-4 at different scan rates.

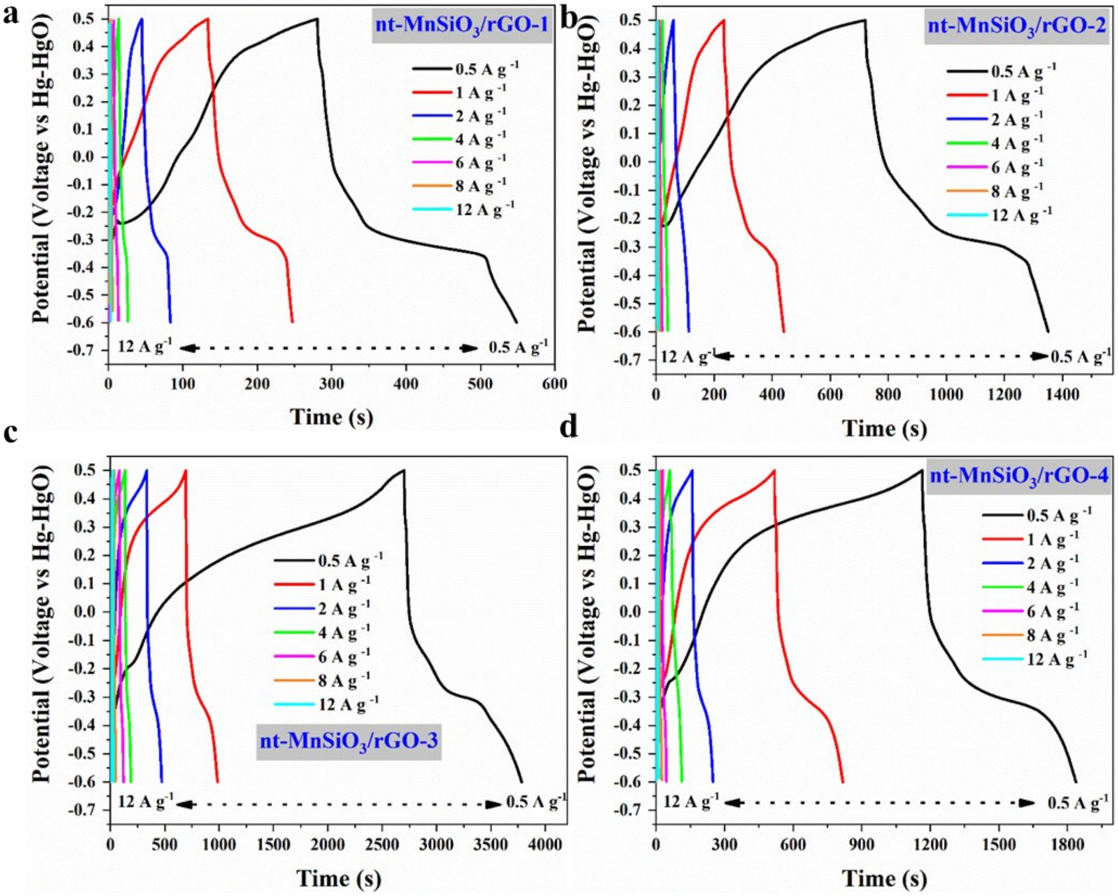

Figure S11. GCD curves of nt-MnSiO$_3$/rGO-1, nt-MnSiO$_3$/rGO-2, nt-MnSiO$_3$/rGO-3 and nt-MnSiO$_3$/rGO-4 at different current densities.

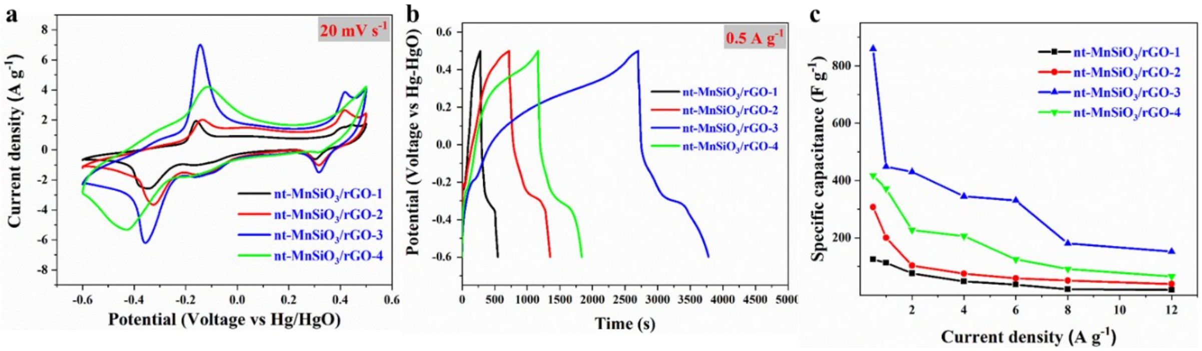

Figure S12. (a) CV curves at 20 mV·s^{-1}, (b) GCD curves at 0.5 A·g^{-1} and (c) the relationship between specific capacitance and current density based on Figure S11 of nt-MnSiO$_3$/rGO-1, nt-MnSiO$_3$/rGO-2, nt-MnSiO$_3$/rGO-3 and nt-MnSiO$_3$/rGO-4.

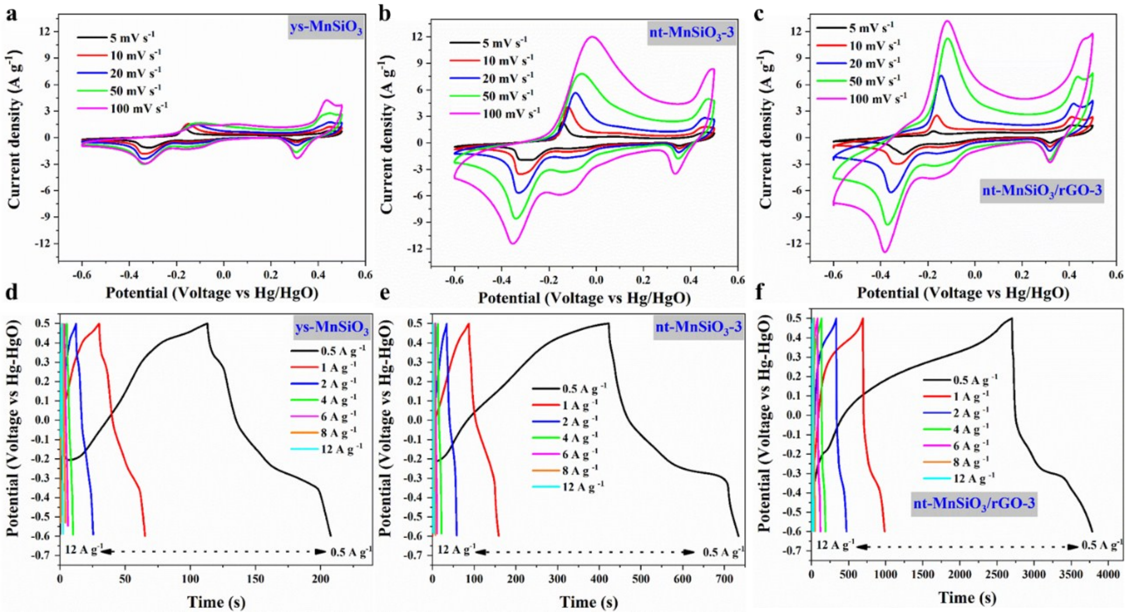

Figure S13. CV curves at different scan rates (a-c) and GCD curves at different current densities (d-f) of ys-MnSiO$_3$ (a, d), nt-MnSiO$_3$-3 (b, e) and nt-MnSiO$_3$/rGO-3 (c, f).

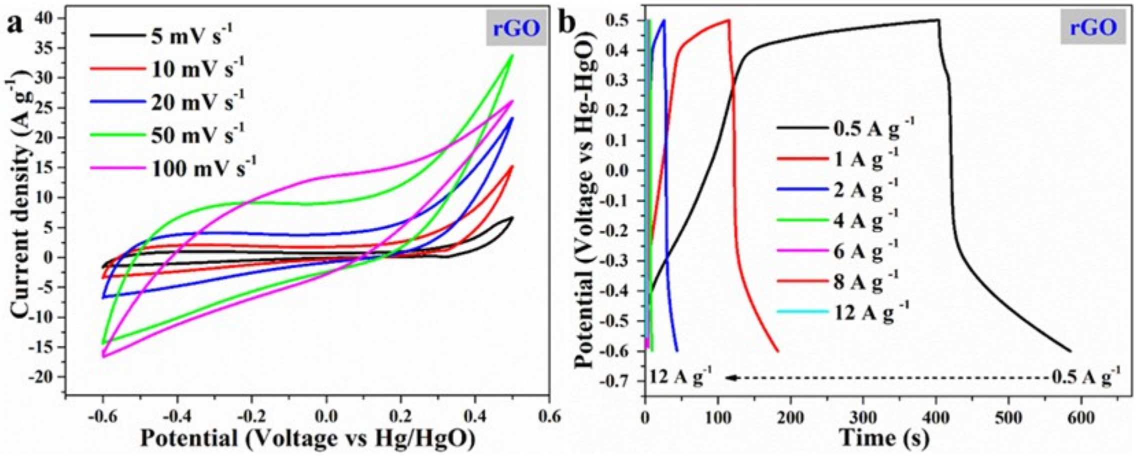

Figure S14. Electrochemical properties of rGO: (a) CV curves at different scan rates, (b) GCD curves at different current densities.

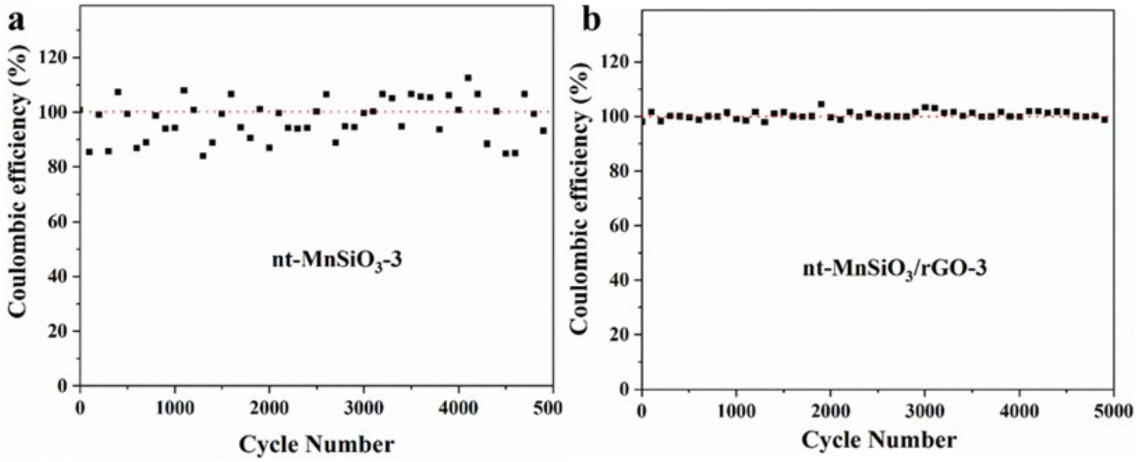

Figure S15. The coulomb efficiency of nt-MnSiO$_3$-3 (a) and nt-MnSiO$_3$/rGO-3 (b) after 5000 cycles.

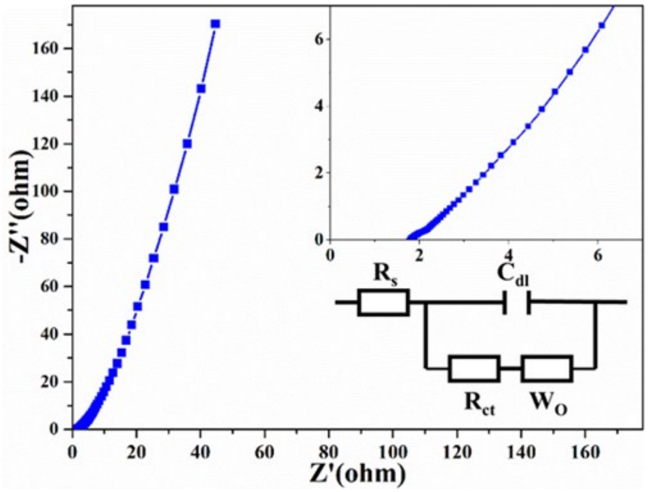

Figure S16. Nyquist plots (EIS spectrum) in the frequency ranging from 100 kHz to 0.01 Hz of nt-MnSiO$_3$/rGO//AC HSC device.

Table S1. Comparison of electrochemical properties of nt-$MnSiO_3$ nanoparticles with manganese silicate based materials reported in the previous literatures.

Types of manganese based materials	Electrolyte	Potential range[V]	$C^{a)}$[F g^{-1}]	$TC^{b)}$[A g^{-1}]	TC[mV s^{-1}]	Retention	Cycle	Ref.
MnSi-C	3 $M^{c)}$ KOH	-1 to -0.3	162.2	0.5	-	85%	10,000	8
Manganese silicate drapes	1 M KOH	-0.5 to 0.4	283	0.5	-	75%	1000	9
Mesoporous-Li_2MnSiO_4	2 M KOH	0 to 0.55	175	-	3	86%	500	10
Crystalline $MnSiO_3$	6 M KOH	-0.6 to 0.5	251	0.5	-	-	-	11
$MnSiO_3$	1 M Na_2SO_4	-0.2 to 1	168.5	0.5	-	-	-	12
$MnSiO_3$/GO	1 M Na_2SO_4	-0.2 to 1	262.5	0.5	-	53%	5000	12
AMSi/MWCNTs	1 M Na_2SO_4	-0.2 to 0.8	236	0.5	-	41%	1000	13
MnSi sphere	3 M KOH	-0.5 to 0.2	517	0.5	-	34%	3600	14
Ys-$MnSiO_3$ sphere	3 M KOH	-0.6 to 0.5	47	0.5	-	-	-	This work
nt-$MnSiO_3$ nanoparticles	3 M KOH	-0.6 to 0.5	167	0.5	-	62%	5000	This work
nt-$MnSiO_3$/rGO	3 M KOH	-0.6 to 0.5	860	0.5	-	80%	5000	This work

$^{a)}$Specific capacitance; $^{b)}$tested condition; $^{c)}$mol L^{-1}

Table S2. Comparison of the electrochemical performance of supercapacitor devices based on manganese silicate based and similar materials.

Types of materials	Electrolyte	Potential range [V]	C[a][mF cm^{-2}]	TC[b][mA cm^{-2}]	C[F g^{-1}]	TC [A g^{-1}]	Retention	Cycle	Energy density[W h kg^{-1}]	Power density[W kg^{-1}]	Energy density[W h m^{2}]	Power density[W m^{2}]	Ref.
MnSi-C//Ni(OH)$_2$ ASC[c]	KOH/PVA[d]	0 to 2	438.5	4	-	-	34%	1000	24.6	604.8	-	-	8
MSi/MWCNTs//AC ASC	1 M[e] Na_2SO_4	0 to 1.8	-	-	146	0.5	81%	1000	131	225	-	-	13
MnSi//AC ASC	KOH/PVA	0 to 1.2	1048.3	2	-	-	32%	900	9.7	-	-	-	14
Carbon-coated Li_2MnSiO_4// AC ASC	1M $LiPF_6$/EC :DMC	0 to 3	-	1	43.2	-	85%	1000	54	150	-	-	15
Li_2MnSiO_4// AC ASC	1M $LiPF_6$/EC :DMC	0 to 3	-	1	43.2	-	-		54	-	-	-	16
C-zinc silicate//AC ASC	PVA/KOH	0 to 2	194.	2	-	-	80%	6900	-	-	0.69	8	17
VO_2(A)//AC ASC	0.5 M Na_2SO_4	0 to 1.5	500	5	-	-	34.6%	1000	-	-	0.714	3.75	18
VO_2(B) solid spheres SSC[f]	1 M Na_2SO_4/CMC	0 to 1.4	122	1	-	-	36%	5000	-	-	0.333	3.5	19
VO_2(B) hollow spheres SSC	1 M Na_2SO_4/CMC	0 to 1.4	246	1	-	-	60%	5000	-	-	0.669	3.5	19
NiSi/GO//AC ASC	PVA/KOH	0 to 1.55	109	1	18	-	71%	5000	6	31.8	0.37	1.94	20
CoNiSi//Ni(OH)$_2$ ASC	PVA/KOH	0 to 1.5	254	0.5	64		82%	10000	20	94.5	0.793	3.75	21
VS4/CNTs SSC	$LiClO_4$/PC	0 to 2.2	676	0.5	-	-	51%	5000	51.2	30.95	-	-	22
$LiNi_{0.5}Mn_{1.5}O_4$/NDG	$LiNO_3$	1.3	-	0.5	72		100%	2300	15	110	-	-	23
RGO/MnOx @$HCN_{0.4}$	KOH	1	-	-	270	1	88%	5000	9.38	500	-	-	24
nt-$MnSiO_3$/rGO/ /AC ASC	PVA/KOH	0 to 1.2	816	1	-	-	87%	2000	40.8	450	1.63	18	This work

[a] specific capacitance; [b] tested condition; [c] asymmetric supercapacitor; [d] polyvinyl alcohol; [e] mol L^{-1}; [f] symmetric supercapacitor

Reference

1. Q. Wang, Y. Zhang, H. Jiang, X. Li, Y. Cheng and C. Meng, *Chem Eng J*, 2019, **362**, 818-829.

2. X. Dong, Y. Zhang, Q. Wang, X. Zhang, M. Gao and M. Changgong, *Dalton Trans.*, 2019, **48**, 11749-11762.

3. M. Chen, Y. Zhang, Y. Liu, Q. Wang, J. Zheng and C. Meng, *ACS Appl. Energy Mater.*, 2018, **1**, 5527-5538.

4. M. J. Zhou, Y. C. Liu, J. Chen and X. L. Yang, *J Mater Chem A*, 2015, **3**, 1068-1076.

5. L. Liang, H. Liu and W. Yang, *J. Alloys Compd.*, 2013, **559**, 167-173.

6. H. Wang, X. Z. Jiang, L. Qian, W. P. Chen and M. F. Zhu, *Advanced Functional Materials (Cmc 2017)*, 2018, DOI: 10.1007/978-981-13-0110-0_80, 723-730.

7. X. L. Liu, Y. F. Gao, R. H. Jin, H. J. Luo, P. Peng and Y. Liu, *Nano Energy*, 2014, **4**, 31-38.

8. Q. S. Wang, Y. F. Zhang, H. M. Jiang and C. G. Meng, *J Colloid Interf Sci*, 2019, **534**, 142-155.

9. H.-Y. Wang, Y.-Y. Wang, X. Bai, H. Yang, J.-P. Han, N. Lun, Y.-X. Qi and Y.-J. Bai, *Rsc Adv*, 2016, **6**, 105771-105779.

10. P. Chaturvedi, A. Kumar, A. Sil and Y. Sharma, *Rsc Adv*, 2015, **5**, 25156-25163.

11. C. Tian, S. Zhao and Q. Lu, *Ceram Int*, 2018, **44**, 17007-17012.

12. Y. Cheng, Y. F. Zhang, Q. S. Wang and C. G. Meng, *Colloid Surface A*, 2019, **562**, 93-100.

13. Q. S. Wang, Y. F. Zhang, S. Z. Jia, Y. H. Han, J. S. Xu, F. Li and C. G. Meng, *Colloid Surface A*, 2018, **548**, 158-171.

14. Q. S. Wang, Y. F. Zhang, H. M. Jiang, X. J. Li, Y. Cheng and C. G. Meng, *Chem Eng J*, 2019, **362**, 818-829.

15. K. Karthikeyan, V. Aravindan, S. B. Lee, I. C. Jang, H. H. Lim, G. J. Park, M. Yoshio and Y. S. Lee, *J Power Sources*, 2010, **195**, 3761-3764.

16. K. Karthikeyan, S. Amaresh, J. N. Son and Y. S. Lee, *J Electrochem Sci Te*, 2012, **3**, 72-79.

17. Y. Zhang, H. Jiang, Q. Wang and C. Meng, *Chem Eng J*, 2018, **352**, 519-529.

18. J. Q. Zheng, Y. F. Zhang, Q. S. Wang, H. M. Jiang, Y. Y. Liu, T. M. Lv and C. G. Meng, *Dalton T*, 2018, **47**, 452-464.

19. Y. Zhang, X. Jing, Y. Cheng, T. Hu and M. Changgong, *Inorganic Chemistry Frontiers*, 2018, **5**, 2798-2810.

20. X. Dong, Y. Zhang, Q. Wang, X. Zhang, M. Gao and M. Changgong, *Dalton Trans*, 2019, DOI: 10.1039/c9dt02415h.

21. Y. Zhang, C. Wang, H. Jiang, Q. Wang, J. Zheng and C. Meng, *Chem Eng J*, 2019, **375**.

22. X. Wang, Y. Zhang, J. Zheng, X. Liu and C. Meng, *J Colloid Interface Sci*, 2019, **554**, 191-201.

23. R. Aswathy, T. Kesavan, K. T. Kumaran and P. Ragupathy, *J Mater Chem A*, 2015, **3**, 12386-12395.

24. M. Liu, M. Shi, W. Lu, D. Zhu, L. Li and L. Gan, *Chem Eng J*, 2017, **313**, 518-526.